ADVANCED MATERIALS INTERFACES
Open Access
www.advmatinterfaces.de

Chemically Reactive Thin Films: Dynamics and Stability

Tilman Richter, Paolo Malgaretti, Thomas M. Koller, and Jens Harting*

Catalyst particles or complexes suspended in liquid films can trigger chemical reactions leading to inhomogeneous concentrations of reactants and products in the film. It is demonstrated that the sensitivity of the liquid film's gas–liquid surface tension to these inhomogeneous concentrations strongly impacts the film stability. Using linear stability analysis, novel scenarios are identified in which the film can be either stabilized or destabilized by the reactions. Furthermore, it is found so far unrevealed rupture mechanisms which are absent in the chemically inactive case. The linear stability predictions are confirmed by numerical simulations, which also demonstrate that the shape of chemically active droplets can depart from the spherical cap and that unsteady states such as traveling and standing waves might appear. Finally, critically discussed the relevance of the predictions by showing that the range of the selected parameters is well accessible by typical experiments.

1. Introduction

In the last decade it has been shown that the dynamics of chemical reactions confined within microdroplets and thin films substantially differ from their bulk counterpart.[1] For example, chemical reactions within droplets occur at rates that are up to $\simeq 10-200$ faster than their bulk counterparts.[2–4] The physical mechanisms responsible for such a speed-up have not been identified yet and indeed they may be multiple at the same time. In fact, when confined within small droplets ($\lesssim 100\mu m$) or thin films,[5] chemical reactions can be affected by different physical phenomena induced by the liquid–liquid interface and even by the three-phase contact line. In these conditions, the chemical reaction may be favored by local surface charges that may enhance the reaction rate.[6–8] At the same time transport phenomena such as enhanced interface diffusion[9] and even Marangoni flows (due to the inhomogeneous surface tension induced by evaporation or varying concentration of chemicals) can lead to a significant speedup of the reactions. In particular, catalytic nanoparticles within water droplets suspended in oil have been shown to induce Marangoni flows since the reaction products act like weak surfactants.[10]

Similarly, thin films have been exploited to enhance chemical reaction yields. For example, model chemical reactions within thin films have shown a ~100 fold enhancement in the conversion efficiency.[11] At the same time, thin films and catalytically active species in the form of dissolved complexes or nanoparticles, are used in Supported Liquid Phase catalysis.[12–14] Within such a framework, the liquid is deposited on a solid support, and molecular catalyst complexes are dissolved in the liquid phase.[15,16] In particular, the latter cases typically involve molecular or particulate catalysts dispersed in the liquid film. Accordingly, the reaction does not proceed uniformly throughout the film and it can lead to local variations in reactant and product concentrations, resulting in solutal Marangoni flows.[17–21] Recently, a novel twist has been represented by Supported Ionic Liquid Phase (SILP) catalysis.[22,23] The concept combines the attractive properties of ionic liquids (ILs), including their tunable physiochemical properties and low sorption, with the benefits of homogeneous and heterogeneous catalysis. Furthermore, the low thickness of the IL film, in order of several nanometers, reduces mass transport limitations. This allows to perform a wide range of industrially relevant reactions such as hydrogenation, dehydrogenation, or hydroformylation.[24–27] However, the stability of IL films within nanopores remains only partially understood.[28,29]

All the above-mentioned examples clearly show that the overall reaction yield strongly depends on the interplay between the coupled dynamics of the catalysts and the liquid interface. However, so far, the study of the stability of thin liquid films has, with a few exceptions,[30–32] focused mainly on the "passive" case, i.e., in the absence of chemical reactions.

Here, we propose a new model capturing the response of thin liquid films to the chemical reactions taking place therein. Our theoretical analysis leads to three main predictions. First, the

T. Richter, P. Malgaretti, J. Harting
Helmholtz Institute Erlangen-Nürnberg for Renewable Energy (IET-2)
Forschungszentrum Jülich
Cauerstr. 1, 91058 Erlangen, Germany
E-mail: p.malgaretti@fz-juelich.de

T. M. Koller
Institute of Advanced Optical Technologies - Thermophysical Properties
Department of Chemical and Biological Engineering and Erlangen Graduate School in Advanced Optical Technologies
Friedrich-Alexander-Universität Erlangen-Nürnberg
Paul-Gordan-Str. 8, 91052 Erlangen, Germany

J. Harting
Department of Chemical and Biological Engineering and Department of Physics
Friedrich-Alexander-Universität Erlangen-Nürnberg
Cauerstr. 1, 91058 Erlangen, Germany

The ORCID identification number(s) for the author(s) of this article can be found under https://doi.org/10.1002/admi.202400835

DOI: 10.1002/admi.202400835

steady-state inhomogeneous distribution of chemicals induced by the chemical reactions may stabilize an otherwise unstable thin film or break it into droplets much smaller than the passive counterpart. Second, depending on the partial accumulation of catalyst at the liquid–gas or solid–liquid interface the chemical reactions can either enhance the rupture by several orders of magnitude or lead to a non-monotonous dependence of the rupture time on the net density of reactants. Third, eventually, the system may attain either a droplet state, whose shape may significantly depart from the spherical cap or even a film with non-uniform height. These complex dynamics are due to the interplay between the gradients in the Laplace and disjoining pressure, induced by variations in the film height, and the Marangoni flows generated by the inhomogeneous concentrations of reactants and products. Our predictions show that all these effects can be controlled by tuning the effective interactions between the catalysts and the interfaces (liquid and solid) as well as by tuning the solubility of reactants and products in the thin film. Remarkably, all these effects can be observed even for weak sensitivity of the liquid–gas surface tension to the composition of the liquid phase (less the 3%) which is well within the range of values that have been determined experimentally in the case of CO_2 or Ar dissolved in ionic liquids.[33]

2. Results

2.1. Model

The dynamics of thin reactive films are quite complex since they involve many physical processes that are all entangled. Focusing on the case of thin films or shallow droplets (i.e., with contact angles $\theta \ll \pi/2$) allows for a simple theoretical description to gain insight into the relevant physical phenomena and to capture the essentials of the underlying dynamics. As such, we can exploit the separation in length scales along the transverse (local film height) and the longitudinal directions. This separation allows us to assume that the liquid pressure p is homogeneous along the direction normal to the solid substrate, i.e., $p(\mathbf{x}, z) = p(\mathbf{x})$.[34,35] Therefore, the problem can be simplified by integrating along the transverse direction leading to the following relevant quantities, namely, the local height of the film $h(\mathbf{x})$ and the densities of catalysts, $\rho(\mathbf{x})$, reactants, $\rho_R(\mathbf{x})$, and products, $\rho_P(\mathbf{x})$ integrated along the direction normal to the solid substrate. Accordingly, the local height of the film is governed by the thin film equation (TFE)[34,35]

$$\partial_t h(\mathbf{x}) = \nabla \cdot \left[\frac{M(h(\mathbf{x}))h(\mathbf{x})}{\mu} \nabla p(\mathbf{x}) - \frac{h^2(\mathbf{x}) + 2bh(\mathbf{x})}{2\mu} \nabla \gamma(\mathbf{x}) \right] \tag{1}$$

Here, $M(h(\mathbf{x}))$ is a height-dependent mobility (see Sections *Model* and A, Supporting Information), and μ is the dynamic viscosity. $\gamma(\mathbf{x})$ is the local liquid–gas surface tension (from now on referred to solely as surface tension) that is assumed to depend on the (vertically integrated) concentration of reactants, $\rho_R(\mathbf{x})$ and products, $\rho_P(\mathbf{x})$,

$$\gamma(\mathbf{x}) = \gamma_0 - \Gamma_P \frac{l}{h(\mathbf{x})} \rho_P(\mathbf{x}) - \Gamma_R \frac{l}{h(\mathbf{x})} \rho_R(\mathbf{x}) \tag{2}$$

where $\Gamma_{R,P}$ account for the sensitivity of the surface tension to the local densities of reactants and products, respectively. The factor $l/h(\mathbf{x})$ underlines that only molecules in the close vicinity of the interface (i.e., up to a molecular length l) affect the surface tension. We remark that the pressure $p(\mathbf{x})$ accounts for both the Laplace pressure as well as for the disjoining pressure (see Sections *Model* and A, Supporting Information). For what concerns the dynamics of the reactant and products, we do not account for any effective interactions with the liquid or solid interface and, due to their fast diffusion (granted by their small size), we assume that their density along the transverse direction is homogeneous. To account for the impact of the varying height of the film on their dynamics we follow the standard Fick–Jacobs scheme[36–39] according to which their integrated densities, $\rho_{P,R}(\mathbf{x})$ obey the following advection-diffusion equations:[40–42]

$$\partial_t \rho_R = \nabla \cdot \left(D_R \nabla \rho_R - v_R \rho_R + D_R \beta \rho_R \nabla \mathcal{F}_0 \right) - \frac{\omega \rho \rho_R}{h} - \sigma_R^{\uparrow} \frac{l}{h} \rho_R + \rho_{R,Res} \sigma_R^{\downarrow} \tag{3}$$

$$\partial_t \rho_P = \nabla \cdot \left(D_P \nabla \rho_P - v_P \rho_P + D_P \beta \rho_P \nabla \mathcal{F}_0 \right) + \frac{\omega \rho \rho_R}{h} - \sigma_P^{\uparrow} \frac{l}{h} \rho_P \tag{4}$$

Here, $D_{R,P}$ are the effective diffusion coefficients of the reactants/products (estimated from the Stokes–Einstein relation), $\sigma_R^{\uparrow}$ denotes the rate at which the reactant is transferred from the liquid film to the surrounding, $\rho_{R,Res}$ represents the concentration of reactants in the gas reservoir, and $\sigma_R^{\downarrow}$ stands for the rate at which the reactant enters the liquid film. The parameter l is a molecular length scale that we introduce to account for the fact that only products located in the upmost molecular liquid layer, of thickness l, are prone to dissolve into the surrounding gas. The chemical reaction occurs with rate ω whenever the reactants are in contact with the catalyst described by its density profile ρ. The effective velocity v_0 accounts for the integrated advective flow (see Section *Model* and Section A, Supporting Information) which in principle may depend on possible (electrostatic) interactions with the fluid and solid interfaces. In order to keep the model simple, in the following, we specialize to the case of no interactions and hence we have $v_R = v_P = \int_0^{h(\mathbf{x})} u(\mathbf{x}, \gamma) d\gamma$ where $u(\mathbf{x}, \gamma)$ is the local velocity profile. The effective potential gradient, $\nabla \mathcal{F}_0 = -k_B T \frac{\nabla h}{h}$ (calculated in the Supporting Information) accounts for the entropic force on the chemical species induced by the inhomogeneous film height[43,44]: thicker films can accommodate for more molecules (per unit support area) than thinner films.

For catalysts, it is well known that, within thin films, they may accumulate at the liquid[45,46] or solid[47] interface, or they may be homogeneously distributed along the film height.[46] Accordingly, we model their effective interactions with the liquid interfaces[48] as

$$\beta \xi(z, h(\mathbf{x})) = \begin{cases} \alpha z & \text{for } \alpha > 0 \\ 0 & \text{for } \alpha = 0 \\ \alpha(z - h(\mathbf{x})) & \text{for } \alpha < 0. \end{cases} \tag{5}$$

Here $\beta := 1/k_B T$ with Boltzmann-constant k_B and absolute temperature T. This potential reflects different scenarios for the distribution of the catalyst within the liquid film along the vertical

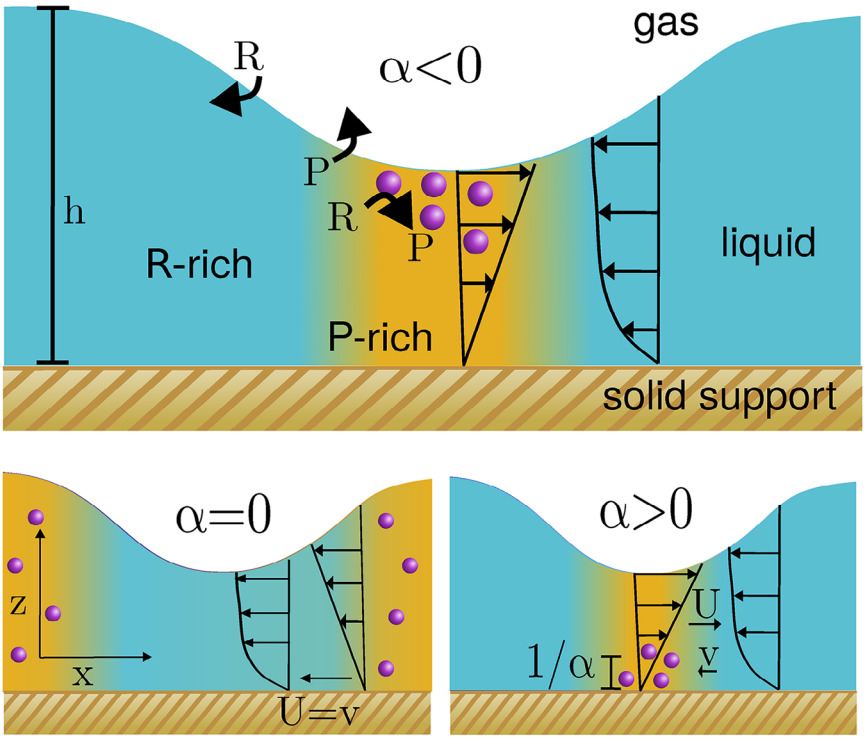

Figure 1. Sketch of the modeled setup. The blue and yellow regions are the liquid film enriched with reactant *R* and product *P*, respectively. The purple dots represent the catalytic particles. Their distribution upon varying the parameter α is shown in the sub-figures. The expected contributions to the flow field are depicted with arrows. *U* represents the flux associated to the liquid height *h* as used in (1) and *v* represents the advection of catalytic particles as defined in (7).

z-direction in the form of an exponential behavior with a characteristic length scale of $1/\alpha$. For $\alpha > 0$ the catalyst is distributed toward the solid substrate while for $\alpha < 0$ it is attracted to the liquid-vapor interface. For $\alpha = 0$, the catalyst is homogeneously distributed along the vertical direction. See **Figure 1** for an illustration of the three cases. As for the chemical species, in order to integrate along the film thickness we follow the Fick–Jakobs[36–38] approximation which, within the length scale separation that we are considering, assumes that the density factorizes in

$$\tilde{\rho}(\mathbf{x}, z) = \rho(\mathbf{x})\tilde{\rho}_z(z, h(\mathbf{x})) \tag{6a}$$

$$\tilde{\rho}_z(z, h(\mathbf{x})) = \frac{e^{-\beta\xi(z,h(\mathbf{x}))}}{\int_0^{h(\mathbf{x})} e^{-\beta\xi(z,h(\mathbf{x}))}} \tag{6b}$$

Accordingly, integrating the advection-diffusion equation along the transverse direction leads to

$$\partial_t\rho(\mathbf{x}) = \nabla\cdot\left(D\nabla\rho(\mathbf{x}) - v_\alpha(\mathbf{x})\rho(\mathbf{x}) + D\beta\rho(\mathbf{x})\nabla\mathcal{F}(\mathbf{x})\right) \tag{7}$$

where *D* is the effective diffusion coefficient of the catalyst in the liquid film (estimated via the Stokes–Einstein relation). The effective potential in (7) is defined as[36–38]

$$\mathcal{F}(\mathbf{x}) = -\frac{1}{\beta}\ln\left(\int_0^{h(\mathbf{x})} e^{-\beta\xi(z,h(\mathbf{x}))}dz\right) \tag{8}$$

that indeed is the local equilibrium free energy of the catalyst. The energy ξ in (8) defines the vertical distribution of the catalyst and is given in Section *Model* of the supporting information. The effective velocity $v_\alpha(\mathbf{x})$ in (7) is related to the integrated flow of catalyst across the transverse direction and it is sensitive to the effective interactions of the catalysts with the interfaces (see supporting information).

2.2. Stability

Thin liquid films of a homogeneous height $h_0 < h_{crit}$ are known to be unstable, i.e. small fluctuations will lead to film rupture and to the formation of droplets. This instability is mainly due to attractive van der Waals forces between the surrounding gas atmosphere and the solid substrate[49,50] which in the current approach are captured by the disjoining pressure $\gamma_0(1-\cos\theta)f(h)$. By standard linear stability analysis about the homogeneous state $h(\mathbf{x}) = h_0$ it is possible to predict the wavenumber of the fastest growing mode of the TFE (1) for $\gamma = \gamma_0 \equiv const.$ to be[51–54]

$$q_{\max,p} = \sqrt{\frac{1}{2}f'(h_0)(1-\cos\theta_0)} \tag{9}$$

Accordingly, even for non-zero contact angles, θ, a thin liquid film with a uniform height h_0 is meta-stable when $f'(h_0) \to 0$ i.e., when the potential f in the disjoining pressure (see Equation S1b, Supporting Information) becomes negligible. For liquids like water,

this happens when h_0 is tens of nanometers.[50] In the ongoing discussion, we assume that the film is thin enough, such that $f'(h_0) > 0$, as this is the relevant scenario for many technological applications including SILP catalysis.[55]

Employing a linear stability analysis (see Experimental Section), the relevant dimensionless numbers can be identified. These are the relative changes in surface tension caused by the presence of the product, $\tilde{\Gamma}_P := \Gamma_P \rho_{0,P} l/(h_0\gamma_0)$, and by the reactants $\tilde{\Gamma}_R := \Gamma_R \rho_{0,R} l/(h_0\gamma_0)$, where $\rho_{0,P}$ and $\rho_{0,R}$ are the equilibrium concentrations of product and reactant given by

$$\rho_{0,R} := \frac{\rho_{R,Res}\sigma_R^{\downarrow}}{\omega\rho_0 + \sigma_R^{\uparrow}} h \tag{10a}$$

$$\rho_{0,P} := \frac{\omega\rho_0}{\sigma_P^{\uparrow}} \rho_{0,R} \tag{10b}$$

as well as the height of the film in units of the "screening length" αh_0. For $\Gamma_P = \Gamma_R = 0$ the chemical reactions have no impact on the film stability. As a reference case, we consider a water film of an initial height $h_0 = 10$nm. The contact angle is set to $\theta_0 = \pi/9 = 20°$. In the following, if not mentioned otherwise, we assume that the sorption rates of the chemicals are equal to the reaction rate at the catalyst. We will discuss the implications of different choices later on. All parameters used are reported in the Experimental Section.

Figure 2 shows the stability portrait of a film that is initially prepared with a homogeneous thickness h_0, and catalyst ρ_0, reactants $\rho_{0,R}$, and product $\rho_{0,P}$ densities for different transverse distribution of catalysts (αh_0, x-axis) and surface tension sensitivity to chemicals (y-axis) where for convenience, we have set $\tilde{\Gamma}_P = 2\tilde{\Gamma}_R$. On the top of the numerical solutions (points), Figure 2 reports also the wavenumber of the fastest growing mode q_{max} normalized by the value $q_{\max,p}$ given by (9) obtained in the absence of chemicals or when chemicals do not affect the surface tension $\Gamma_P = \Gamma_R = 0$ (color code). In particular, five different scenarios can be identified: (1) the film is stabilized by the chemical reactions (green dots and dark brown background), (2) the film breaks as "passive" meaning in a very similar as if there was not chemical reaction happening (red stars and light brown/cyan), (3) a crossover region between the former two where the simulation time and system size are insufficient to observe film rupture (pink triangles), (4) the film breaks with much shorter wavelengths as compared to the "passive" case (magenta stars and blue background) and (5) short wavelength excitement but no film-rupture (orange triangles and blue background).

The linear stability analysis indicates that when the catalyst particles are preferentially at the vapor-liquid interface ($\alpha h_0 \leqslant 0$), the thin film is stable (green dots) when

$$\tilde{\Gamma}_P + \tilde{\Gamma}_R > \frac{\Gamma_c(\rho_{0,P} + \rho_{0,R})l}{(h_0\gamma_0)} \tag{11}$$

where $\Gamma_c(\rho_{0,P} + \rho_{0,R})l/(h_0\gamma_0) = 1 - \cos\theta_0$ is the threshold value that is determined by the reduction in the surface tension due to both reactants and products and closely resembles the amount of surfactants needed to stabilize an otherwise unstable film.[40] When (11) is not fulfilled (red stars) the thin film is unstable and

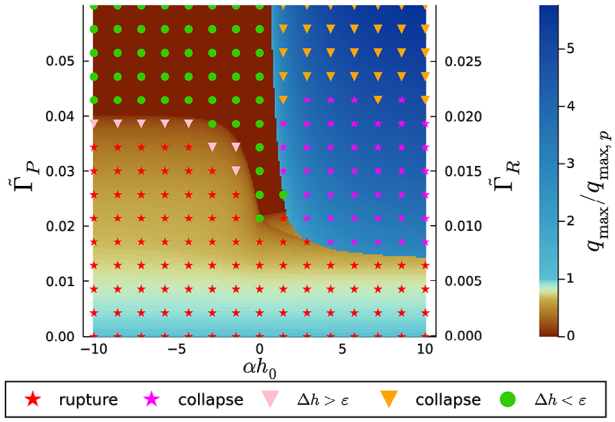

Figure 2. Representation of the fastest growing wave mode/vector of the studied thin film system in terms of the percentage changes in the vapor-liquid surface tension due to the presence of the reaction product, $\tilde{\Gamma}_P := \Gamma_P \rho_{0,P} l/(h_0\gamma_0)$, and reactant $\tilde{\Gamma}_R := \Gamma_R \rho_{0,R} l/(h_0\gamma_0)$, for varying concentration distribution of the catalyst particles in vertical direction, αh_0. The colormap in the background indicates the wavenumber of the fastest growing mode of the system obtained from (16). The dots in the foreground give the eventual state of a numerical solution of Equations (1–4) and (7) after 10^9 iterative time steps. Stars represent simulation results where the initially closed film forms droplets. Triangles represent still closed films with excitation δh higher than a certain threshold ϵ, while green dots correspond to an excitation δh below that threshold ϵ. The colors differentiate between simulations that are driven by the accumulation of catalyst (magenta and orange), called the collapse regime, or by the passive dynamics of the thin film (red and pink). The parameters and properties are the same as listed in the Experimental Section. The symbols and colors used for the numerical simulation agree with the ones used in Figure 4.

the fastest growing mode is characterized by $q_{\max,p} > q_{\max} > 0$. Now, in the same way as in the passive case, the homogeneous system is not stable which leads to the rupture of the liquid film. The resulting droplets in this case are larger than in the passive case. **Figure 3a** shows an example of a simulated flow field in this regime leading to film rupture.

When the catalytic particles are homogeneously distributed ($\alpha \approx 0$), significantly less catalytic activity is required to stabilize the system, as can be seen in Figure 2. This is because, for a homogeneous distribution, both advection and diffusion enforce a strong correlation between the film height and the catalyst density, i.e., $\rho \propto h$. For advection this can be seen from the effective mobilities of the catalyst, M_p, M_γ (see Equation S13, Supporting Information), and film height, M, $(h + 2b)/2$ (see (1)). The mobilities become pairwise equal, $M_p = M$ and $M_\gamma = (h + 2b)/2$ and this causes the catalytic particles to move along with the liquid. Concerning diffusion, for $\alpha = 0$, $\nabla\mathcal{F} = -k_B T \nabla h/h$ and thus, at equilibrium, ρ is proportional to h. This proportionality stemming from both diffusion and advection, $\rho \propto h$, leads to enhanced consumption of reactant (and catalysis of products) proportional to h. In this way, variations in film height are suppressed by locally decreasing the surface tension due to the chemical reactions. Such behavior is already captured by the LSA as terms with the prefactors M_p or M_γ have a counterpart with prefactor M or $(h + 2b)/2$ canceling each other out (see Supporting Information, Section A).

Finally, for $\alpha > 0$, the catalysts are accumulated at the solid–liquid interface. Considering small surface tension effects

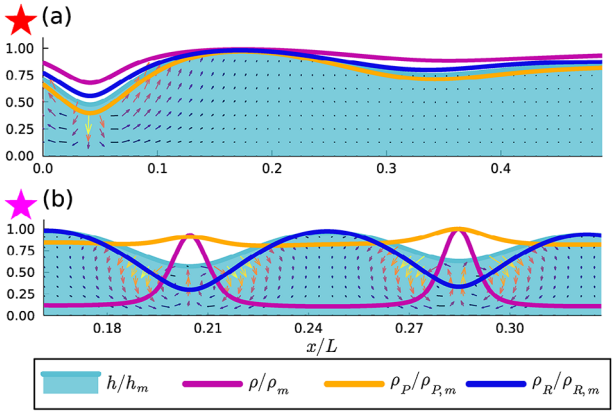

Figure 3. The height h, catalyst density ρ, product density ρ_P and reactant density ρ_R normalized by their respective maxima h_m, ρ_m, $\rho_{P,m}$ and $\rho_{R,m}$ for a snapshot shortly before film-rupture of the spinodal regime (a) and the collapse regime (b). The flow field is interpolated from surface tension and pressure gradient $\nabla\gamma$, ∇p assuming incompressibility $\partial_x u + \partial_z v = 0$. Arrows indicate the direction of the flow and their color the magnitude of the local velocity. The lengths of the arrows do not scale the same among the two insets, i.e., the velocity field in (a) is exaggerated 10 times more than in (b). The simulations reported here correspond to the magenta and red stars in Figure 4.

$\tilde{\Gamma}_P, \tilde{\Gamma}_R \ll 1$ we observe that the wavenumber of the fastest growing mode is reduced as compared to the passive case wavenumber $q_{\max}$, $q_{\max,p}$ (cyan to brown background in Figure 2). This stems from the reduction in surface tension by the presence of the chemicals. In contrast, for larger values of $\tilde{\Gamma}_P, \tilde{\Gamma}_R$ the wavenumber of the fastest growing mode becomes larger than the passive wave number, $q_{\max} > q_{\max,p}$ (dark blue background in Figure 2), indicating the excitation of short wavelengths. The mechanism underlying this phenomenon can be explained as follows: Under the assumptions that $\alpha \gg 0$ and $\Gamma_P, \Gamma_R \gg 0$ (i.e., the catalytic particles are highly accumulated near the solid substrate, and the surface tension is lower in the product-rich phase than in the reactant rich phase, see Figure 1), a high local concentration of catalyst at a point in space $\mathbf{x}$ locally reduces surface tension. This reduction leads to the creation of surface stress, inducing a Marangoni shear flow $\nabla\gamma(h+2b)/(2\mu)$ away from the area of high catalyst concentration. Consequently, the film height at that location decreases, forming a corrugated vapor-liquid interface with a radius of curvature R. This corrugation generates a Laplace pressure γ/R, resulting in a parabolic-shaped flow $\nabla pM(h)/\mu$ toward the area of high catalyst concentration. These two contributions, along with the disjoining pressure, sum up to form the height-averaged velocity U (compare with Equation (2) in the supporting information). According to Equation (7), the catalyst particles experience an effective flow with the velocity $v = \nabla\gamma M_\gamma/\mu + \nabla pM_p/\mu$, while the film height h is affected by the flow with the velocity U. Because the Marangoni flow and the pressure gradient-driven flow have distinct flow profiles (as depicted in Figure 1), it is possible that U and v have different directions. Consequently, the film corrugation persists, since the flow related to U transports liquid away from the regions of high concentration, while the pressure-driven flow related to v accumulates more catalyst at that location. This effect is illustrated by the the flow field of an exemplary simulation in this regime as shown in the lower inset of Figure 3. The presence of such rollers or vortices in thin liquid films in the presence of Marangoni flows has been observed before for thermal gradients.[56] Similar phenomena have been observed in the context of the Keller–Segel model,[57] in whose spirit we refer to this effect as a "collapse."

Upon raising α above $\alpha = 0$ there is a jump discontinuity from $q_{\max} = 0$ to $q_{\max} \gg q_{\max,p}$ (Figure 2, brown to blue background). Also when raising $\tilde{\Gamma}_P + \tilde{\Gamma}_R$ a jump discontinuity from smaller $q_{\max}$ to higher $q_{\max}$ can be observed at roughly $\tilde{\Gamma}_P + \tilde{\Gamma}_R \approx 0.015 + 0.0075$ (Figure 2, light brown background to blue background). Analyzing the eigenvalues of the linearized system (refer to Figure S5, Supporting Information), we observe that the two physical effects connected with the disjoining pressure and the collapse, are associated with local maxima in dispersion relation $\eta_m(q)$ (see Experimental Section). The observed jump in the fastest-growing modes can be explained by the global maximum switching from one local maximum to the other. In particular, as shown in Figure S5 (Supporting Information), the dispersion relation undergo a significant change upon increasing the parameters $\Gamma_{R,P}$: for small and large values of $\Gamma_{R,P}$ the stability portrait resemble that of conservative systems with a fastest growing mode for a finite wavelength and the zero mode marginally stable. Such a stability portrait allows for coarsening dynamics since all the modes with wavelength larger than the fastest growing mode are excited. For intermediate values of $\Gamma_{R,P}$ the stability portrait changes toward a "Turing-like" pattern where long wavelengths are suppressed. Interestingly, such a behavior has been observed also in the case of deformable membranes.[58]

Finally, for $\tilde{\Gamma}_P + \tilde{\Gamma}_R = 0$, where no effect of the product and reactant concentration on the surface tensions is given, we find $q_{\max} = q_{\max,p}$, as expected.

2.3. Rupture

After reporting on the onset of the instability, we now turn to the dynamics leading to the breakage of the film. **Figure 4** shows the time evolution of the height difference $\Delta h = \max h - \min h$ for some representative cases. When the thin film is stabilized by the chemical reactions (green points) or the chemical reactions are almost irrelevant (red stars) the dynamics of the system toward the steady state are relatively simple (see Figure 4). This is confirmed by the fact that the time evolution obtained by the numerical simulations agrees well with the linear solution (16): the amplitude of the dominant wavelength $(1/q_{\max})$ approaches exponentially its steady-state value. Only as the system approaches the steady state, the linear solutions (16) become less accurate. At variance, for red and pink stars, the chemical reactions are more relevant and indeed the time evolution cannot be captured fully by the linearized equations as for the simpler cases.

Initially, the amplitudes grow as predicted by (16), constructing the wavemode with wavenumber $q_{\max}$. Yet, at a certain point in time, this growth halts, and the full numerical solution no longer aligns with (16). In such cases, the rupture of the film cannot occur at such small wavelengths $(1/q_{\max} \ll 1/q_{\max,p})$. Instead, the system's maxima merge, giving rise to larger dominant wavelengths that are not predicted by the LSA. An example of such a simulation can be observed in Figure S2 as well as in the Video S3 (Supporting Information).

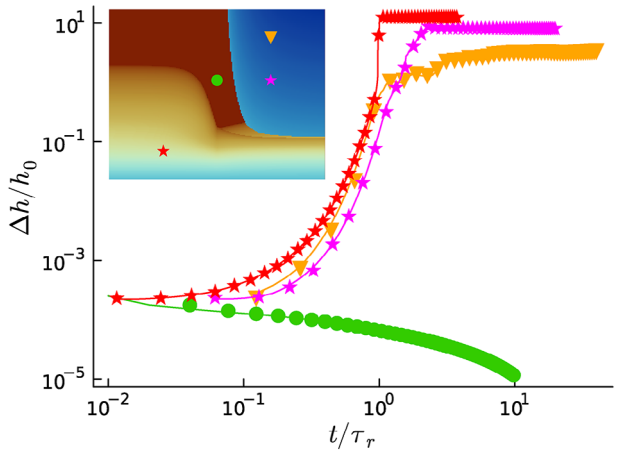

Figure 4. The maximum height $\Delta h/h_0 = (\max h - \min h)/h_0$ difference in time plotted for four exemplary simulations, showing the different possible behaviors of the system. All simulations are started in the perturbed homogeneous state $h = h_0 + \epsilon\mathcal{N}_0^1$, $\rho = \rho_0$, $\rho_A = \rho_{0,A}$, $\rho_B = \rho_{0,B}$. In the inset, we show the position of those simulations in the stability diagram Figure 2 as colored symbols. For every simulation, a video is available in the supporting information. In the simulation shown with green dots, $\tau_r = \infty$ thus we choose an arbitrary value instead, to show its evolution in the same plot as the other three. For the axis labels of the inset see Figure 2. The symbols and colors used here match the ones in Figure 2.

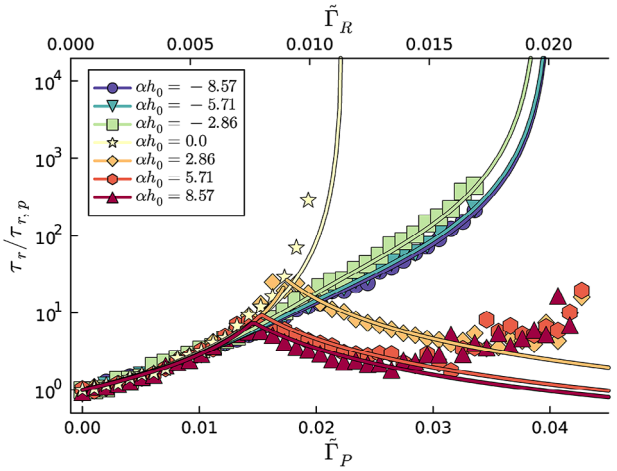

Figure 5. The rupture time of a liquid film containing catalytic particles normalized by the passive case rupture time $\tau_{r,p}$ of a thin liquid film is plotted as a function of the percentage change of surface tension at a mean concentration of product $\tilde{\Gamma}_P$ or reactant $\tilde{\Gamma}_R$ (on the lower or upper **x**-axis, respectively) and vertical distribution of catalyst αh_0 (color code). The solid lines refer to the rupture time expected from the linear solution by (14), while stars are obtained from a numerical solution of Equations (1–4) and (7) starting from a homogeneous initial condition with a small initial random perturbation. All relevant parameters are chosen as listed in the Material and Methods section.

For $\tilde{\Gamma}_P + \tilde{\Gamma}_R > \Gamma_c(\rho_{0,P} + \rho_{0,R})l/(h_0\gamma_0)$, (orange down-triangle) we also observe the initial growth of the dominant wavelength $1/q_{\max}$, that is followed by a coarsening unifying the maxima of the concentration of catalyst ρ. In this situation, the surface tension γ is very low and Young's law of wetting predicts a contact angle of $\theta = 0$. Thus no film rupture occurs even though certain wavelengths of the system are excited by the dynamic interaction of chemical reactions and surface tension.

To quantitatively capture the dependence of the rupture dynamics on the chemical reactions we define the rupture time τ_r as the earliest time when the film height somewhere becomes as small as the precursor height h^*,

$$h(\mathbf{x}, \tau_r) = h^* \tag{12}$$

which captures the time it takes the homogeneously initialized thin film to undergo rupture and evolve into droplets. A good estimate on τ_r is provided by the linearized solution (16)

$$\tau_r = \frac{1}{\eta_m(q_{\max})} \ln \frac{h_0}{\epsilon} \tag{13}$$

It turns out that this is well described by the characteristic time of the system $1/\max(\eta_m(q))$ where η_m is the largest eigenvalue of the dispersion relation $A(q)$ (see Section A, Supporting Information). We write the rupture time in a normalized form by referencing the rupture time $\tau_{r,p}$ for the passive case $\Gamma_P = \Gamma_R = 0$, i.e.,

$$\frac{\tau_r}{\tau_{r,p}} \approx \frac{\max \eta_{m,p}(q)}{\max \eta_m(q)} \tag{14}$$

where $\eta_{m,P}$ is the largest eigenvalue of the dispersion relation for the pure liquid. **Figure 5** shows the estimates given by (14) (solid lines) as well as the rupture time obtained from numerical simulations (symbols). The parameters are chosen as shown in the Experimental section. At $t = 0$ all the fields are initialized homogeneously plus a small random perturbation in the liquid height ($h = h_0 + \epsilon\mathcal{N}, \rho = \rho_0, \rho P = \rho_{0,P}, \rho_R = \rho_{0,R}$) for a random variable $\mathcal{N}$.

We observe in Figure 5 that for $\tilde{\Gamma}_P + \tilde{\Gamma}_R \lesssim 0.0225$ all data collapses onto a master curve. For $\Gamma_P = \Gamma_R = 0$, we retrieve the passive case and thus $\tau_r/\tau_{r,p} = 1$. Considering $\tilde{\Gamma}_P + \tilde{\Gamma}_R \gtrsim 0.0225$, the situation becomes more complex. For $\alpha < 0$, in general the rupture time rises with $\tilde{\Gamma}_P + \tilde{\Gamma}_R$ until it reaches a threshold value $\Gamma_c(\rho_{0,P} + \rho_{0,R})l/(h_0\gamma_0)$ where $\tau_r \to \infty$ which corresponds to the stabilization of the homogeneous film. For $\alpha \ll 0$, that threshold value is as discussed before $\Gamma_c(\rho_{0,P} + \rho_{0,R})l/(h_0\gamma_0) = 1 - \cos\theta_0$. For $\alpha \approx 0$, the rupture time τ_r diverges for a smaller value of $\tilde{\Gamma}_P + \tilde{\Gamma}_R$. In the case of $\alpha > 0$, the rupture time initially increases with growing $\tilde{\Gamma}_P + \tilde{\Gamma}_R$ until it begins to decrease once more. This non-monotonous behavior corresponds to the transition from the unstable film (red stars in Figure 2) to the collapse (magenta stars in Figure 2) regime, where the largest eigenvalue of the dispersion relation η_m (see Experimental Section) starts growing as $\tilde{\Gamma}_P + \tilde{\Gamma}_R$ increases. Despite the jump discontinuity in the transition of $q_{\max}$ to the collapse regime, $\max(\eta_m)$ and τ_r exhibit continuity at the transition point for larger values of α. This can be understood by considering the eigenvalue η_m as shown in Figure S5 (Supporting Information). Concerning the reliability of the predictions of the LSA, Figure 5 shows good agreement of the rupture time predicted by the linearized solution (14) (lines) with the simulations (symbols). We note that such an agreement is remarkable since the rupture occurs outside the linear regime

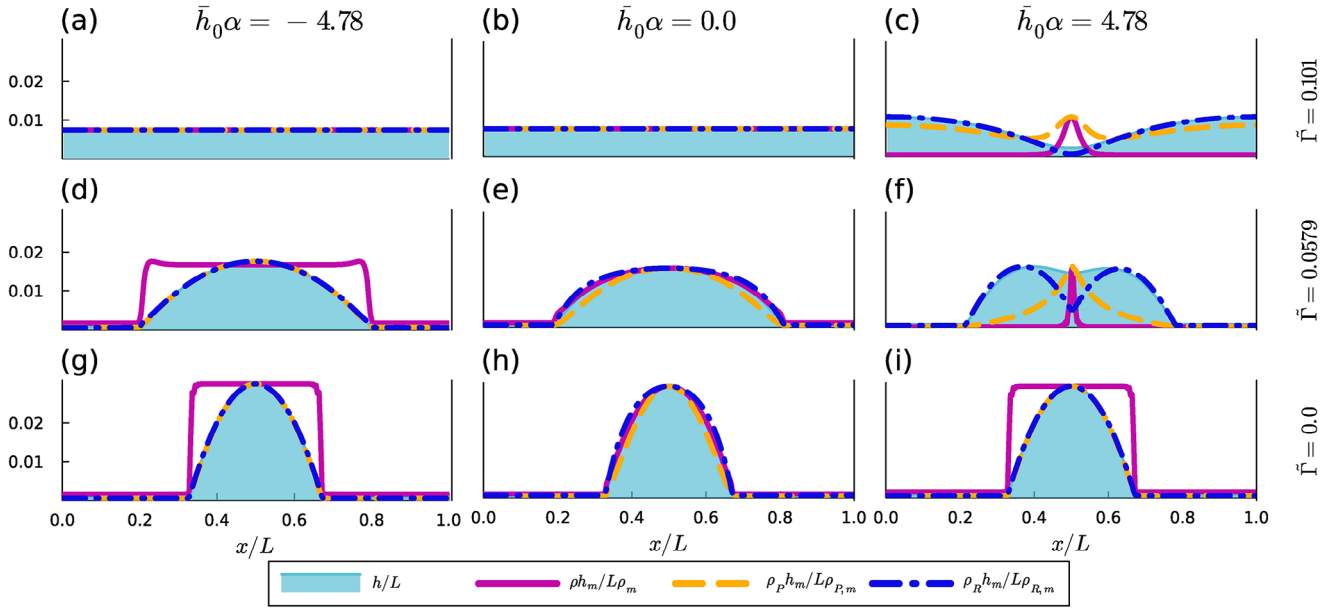

Figure 6. Steady state of a droplet with dissolved active catalyst particles for different parameters $\bar{h}\alpha$ and $\tilde{\Gamma} := (\Gamma_P\bar{\rho}_{0,P} + \Gamma_R\bar{\rho}_{0,R})l/(\gamma_0 h_0)$, representing the assumed vertical distribution of catalyst over a length scale $1/\alpha$ and the percentage change of the surface tension according to (2). As initial conditions we choose $h(0)$ a spherical cap with contact angle θ_0, $\rho(0) \equiv$ for $h(0) > h^*$ and $\rho(0) \equiv 0$ for $h(0) \leqslant h^*$. The density of reactant is initially chosen as $\rho_R(0) = \rho_{R,Res}\sigma_R^{\downarrow}h(0)/(\omega\rho(0) + \sigma_B^{\uparrow}l)$ and the product density is $\rho_P = \omega\rho(0)\rho_R(0)/(l\sigma_P^{\uparrow})$. Negative α corresponds to the catalyst being enriched at the liquid-vapor interface, $\alpha = 0$ to a vertically homogeneous distribution of catalyst, and positive α indicates that catalyst is enriched close to the solid substrate (see Figure 1). The concentration fields ρ, ρ_P, and ρ_R are divided by their respective maxima ρ_m, $\rho_{P,m}$, $\rho_{R,m}$ and multiplied by the maximum height of the system h_m to visualize all fields in a single plot. The lengths are normalized by the system size L. We run the simulations until no difference between two consecutive dumps until full convergence. The aspect ratio in all insets is fixed to 10.

where (16) used for the calculations in the LSA framework is not valid anymore. However, the LSA, via the ansatz in (16), still qualitatively captures the timescale reasonably well. Quantitatively, the rupture time of the simulations does not match (14) anymore for $\tilde{\Gamma}_P + \tilde{\Gamma}_R \gtrsim 0.045$ and $\alpha > 0$. This is due to the wavenumber of the fastest growing mode becoming large here, i.e., the dominating wavelength is very small. The dominant wavelength builds up, but the thin film cannot break at such small wavelengths. Larger wavelengths have to grow for film rupture to occur. This process happens outside of the linear regime and is well illustrated by the data set represented by magenta stars in Figure 4 as well as in Figure S2 and the corresponding Video S3 (Supporting Information). Film rupture in this case is not associated to the fastest growing wavenumber but to a smaller one.

2.4. Droplets

Finally, once the film is broken droplets are formed. To reduce the required computing time when investigating the steady state of droplets containing active catalytic particles, we start our simulations from a spherical cap, i.e., a portion of a sphere cut off by a plane (The spherical cap is the expected equilibrium shape of a liquid droplet with a radius smaller than the capillary length $r_c = \sqrt{\gamma_0/(\rho_l g)}$, where g is the gravitational constant[50]). The contact angle of this cap on the solid substrate is initially chosen as θ_0, and the initial densities ρ, ρ_P, and ρ_R are chosen constant inside the droplet i.e. $\rho(\mathbf{x}, 0)$, $\rho_P(\mathbf{x}, 0)$, $\rho_R(\mathbf{x}, 0) = C$ where $h(\mathbf{x}, 0) > h^*$ and $\rho(\mathbf{x}, 0)$, $\rho_P(\mathbf{x}, 0)$, $\rho_R(\mathbf{x}, 0) = 0$ for $h(\mathbf{x}, 0) = 0$. **Figure 6** shows the droplet shape and the density of catalyst as well as of the chemicals for the three different scenarios, captured by α, and for the same parameter values used in Figure 2.

Due to their large diffusion coefficients compared to the catalyst's diffusion coefficient and vertically homogeneous concentration distribution, the products and reactants are homogeneously distributed across the film. For larger values of Γ_R, Γ_P this leads to an overall decrease of the liquid-vapor surface tension and hence eventually to a perfectly wetting film (panels (a–c) in Figure 6). For smaller values of Γ_R, Γ_P, the decrease in γ is not sufficient, and the droplet persists (panels (d–i) in Figure 6). Interestingly, in these cases, the liquid-vapor surface tension is not homogeneous anymore and it induces a weak Marangoni flow toward the contact lines that leads to a slight accumulation of catalyst at the three-phase contact line.

For $\alpha \ll 0$, catalyst particles accumulate at the liquid interface, and hence they behave as an effective $(d-1)$-dimensional ideal gas, spread homogeneously across the droplet (Figure 6a,d,g). Upon raising values of the strength of the surface tension effects Γ_P, Γ_R, the surface tension gets reduced, and the droplet spreads (Figure 6d) eventually leading to the liquid becoming perfectly wettable. Thus, the droplet becomes a homogenous closed film (Figure 6g).

For a homogeneous catalyst distribution, $\alpha = 0$, at steady state, all the densities are proportional to the droplet height h. Accordingly, the surface tension is homogeneous everywhere (Figure 6b,e,h). As before, upon raising values of the strength of the surface tension effects Γ_P, Γ_R, the surface tension lowers,

leading to the spreading of the droplet (e) and eventually to a perfectly wetting liquid film (b).

For $\alpha \gg 0$, the catalytic particles accumulate at the solid substrate. In this case, the eventual distribution of the catalyst is very sensitive to $\Gamma_{R,P}$, for small values of $\Gamma_{R,P}$ an effective $(d-1)$-dimensional homogeneous layer is formed at the bottom of the film (Figure 6i). For larger values of $\Gamma_{R,P}$ (and symmetric initial conditions, see Supporting Information), the catalysts accumulate (Figure 6f). Similarly to the collapse of the catalyst observed in the initially homogeneous system, the Marangoni flows generated by a locally lower vapor-liquid surface tension at the location of high catalyst concentration deform the droplet, creating a pressure that pushes the catalyst toward the center. The product becomes enriched in the presence of more catalysts, and vice versa for the reactant. The concentration of catalyst at the droplet's center is similar to that observed in Ref. [10] where catalytic TiO_2 heavy micro-particles (thus, $\alpha > 0$) inside a liquid droplet of 3% H_2O_2 solution, accumulate at the center of the droplet. We mention that the relative position of the catalyst's maximum density and the droplet height depends on the initial conditions (see Figure S4, Supporting Information). Finally, for even larger values of $\Gamma_{R,P}$ the liquid-vapor surface tension γ gets, according to our model, so low that the liquid becomes perfectly wetting, and thus the droplets spread over the periodic boundary of the simulation box forming a closed film (Figure 6c). However, for $\alpha > 0$, the accumulation of catalyst persists, leading to an inhomogeneous film thickness.

2.5. Sorption and Strength of Surface Tension Effects

In the following, we analyze the dependence of the phenomena that we discussed so far on the ratio of the surface tension sensitivity to chemicals $\Gamma_P\rho_{0,P}/\Gamma_R\rho_{0,R}$ and on the rates of sorption $\sigma_P^{\uparrow}l/\omega\rho_0 = \sigma_R^{\uparrow}l/\omega\rho_0$. Indeed, as shown in **Figure 7**, the stability diagrams, like the one in Figure 2, are sensitive to these ratios.

There are three types of stability diagrams predicted by the LSA.

First, some diagrams are shaped as the one presented in Figure 2 (framed in dark or light green, where the dark green framed diagram corresponds to the one shown in Figure 2) as discussed in the previous sections.

Second, for equally strong surface tension effects of product and reactant $\Gamma_P\rho_{0,P}/\Gamma_R\rho_{0,R} = 1$ and sorption rates are equal to the reaction rate $\sigma_P^{\uparrow}/\omega\rho_0 = \sigma_R^{\uparrow}/\omega\rho_0 = 1$ (central diagram framed in red). Here, reactants and products equally affect the surface tension, and they have the same sorption. Accordingly, due to the symmetric roles of reactants and products, the fastest-growing mode is independent of the vertical distribution of catalyst α. Stability is reached when Equation (11) holds. Thus, the catalyst can be effectively treated as a simple surfactant or solute, lowering the surface tension of the liquid. By Equation (10) $\sigma_P^{\uparrow}/\omega\rho_0 = 1$ implies that $\rho_{0,P} = \rho_{0,R}$ and thus one obtains $\Gamma_P = \Gamma_R$ from $\Gamma_P\rho_{0,P}/\Gamma_R\rho_{0,R}$. Whenever $\Gamma_P = \Gamma_R$ holds, the stability portrait looks like the one reported framed in red. For all other diagrams reported here $\rho_{0,P} \neq \rho_{0,R}$ and $\Gamma_P \neq \Gamma_R$.

The third regime occurs for $\sigma_P^{\uparrow}/\omega\rho_0 = \sigma_R^{\uparrow}/\omega\rho_0 = 0.1$ (framed in blue). Here the homogeneous state is never stable, at least not for the parameter range studied here. However, as we will discuss later using numerical simulations, this does not necessarily indicate film rupture. In the third type of stability diagram, we observe a second collapse mechanism in the left corner (high surface tension effects and catalyst enriched at the liquid surface) of each diagram. Here the collapse is caused by catalyst enriched at the liquid surface ($\alpha < 0$) effectively raising the local surface tension by consuming reactants and creating products. Therefore the Marangoni flow points from regions of low catalyst concentration to regions of higher catalyst concentration accumulating the catalyst. The catalyst behaves as if it were an "anti-surfactant."

Furthermore, we obtain complex eigenvalues of the dissipation relation in the right corner of those diagrams framed in blue, predicting a phase shift of excited wave modes with time in the linear regime. The black lines indicate the onset of such complex eigenvalues, where above the line significant imaginary parts appear in the eigenvalues of the dispersion relation. Finally, for $\Gamma_P\rho_{0,P}/\Gamma_R\rho_{0,R} = 1/2$ and $\sigma_P^{\uparrow}/\omega\rho_0 = \sigma_R^{\uparrow}/\omega\rho_0 = 1$ (framed in cyan) we observe a transition between a stability portrait of the first type and one of the third type.

Numerical simulations show the onset of eventual regimes that are not present in Figure 2, including film-rupture, inhomogeneous film height with no film rupture, as well stable films with homogeneous height $h \equiv h_0$. For the films that break into droplets, we can distinguish between spherically shaped droplets obtained either via spinodal rupture (red stars, panel (g)) or via collapse (magenta stars, panel (h)), as well as droplets where the chemical concentration fields are shaped by the second kind of collapse, being catalyst enriched at the liquid interface and behaving as an effective "anti-surfactant" by consuming surface active reactant and replacing it with less surface active product (red up-triangles, panel (f)).

For films that do not break, on top of films with homogeneous height (green circles), we observe films with inhomogeneous height. This is associated with local inhomogeneity in the chemical concentrations and the resulting flow dynamics. Of such steady states there are the ones resulting from the collapse mechanism discussed before (orange down-triangles, panel (e)) where the catalyst concentration is the highest where the film height is lowest and vice versa. Furthermore, patterns are emerging from the second collapse mechanism (orange up-triangles, panel (a)) that are characterized by a matching of the maxima of film height and catalyst concentration. On top of that, we observe not-ruptured perturbed states without any collapse for $\alpha = 0$ (orange squares, panel (b)). Finally, for some parameters, we observe traveling waves (In Figure 7c, a right moving pattern is shown, but left moving patterns can be observed as well.) (orange right-triangles, panel (c)) and stationary waves (orange diamonds, panel (d)). These numerical results are supported by the LSA which shows non-zero imaginary components in the eigenvalues (above the black lines).

2.6. Catalytic Yield

Our theoretical predictions highlight the role of the distribution of catalysts across the film thickness. However, for catalytic devices, the most interesting number is the catalytic yield, i.e., the actual output of product of the system. To assess this number, we measure from simulations the amount of product that is evaporated from the liquid film into the gas atmosphere. This is given

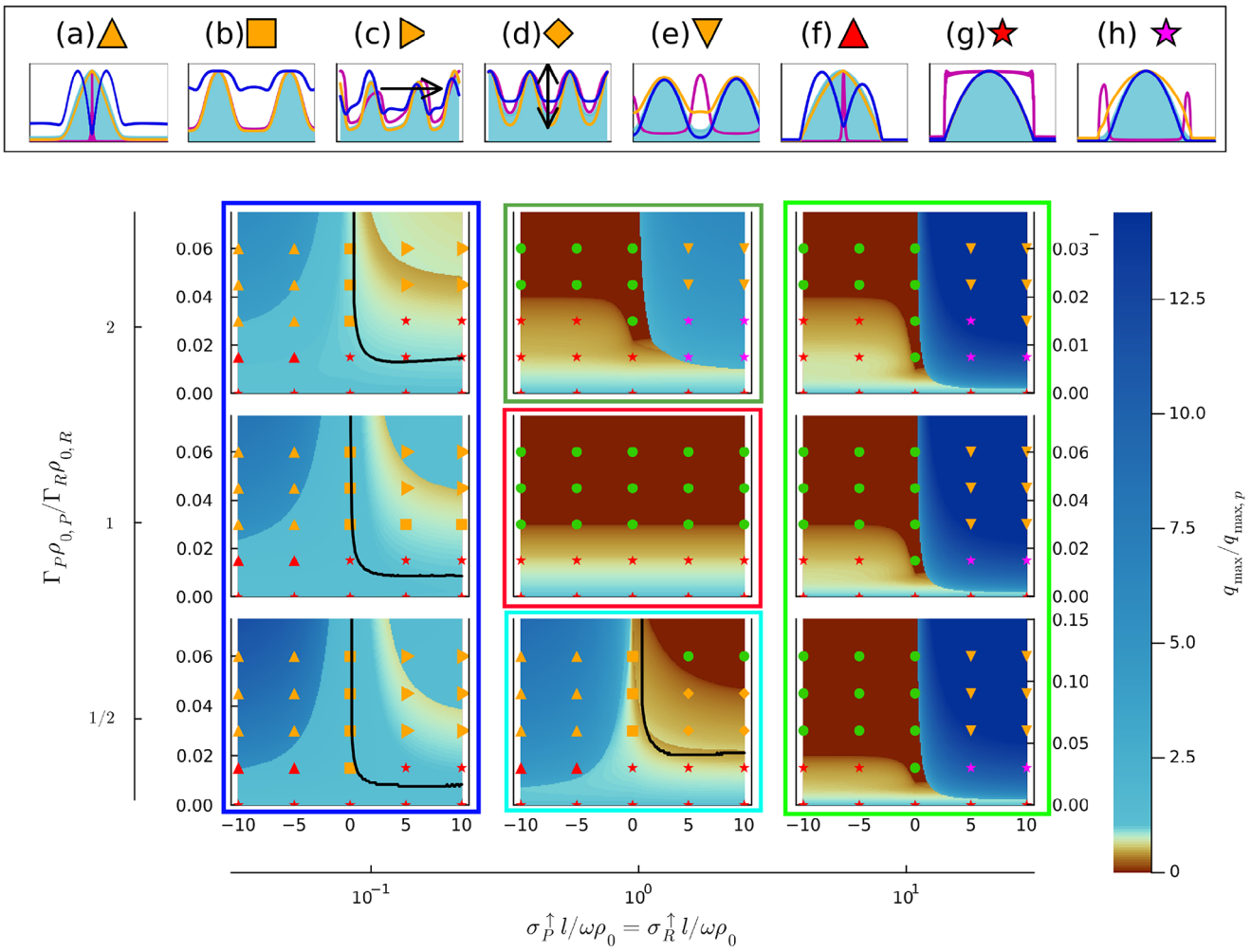

Figure 7. Stability diagrams depending on sorption rates of product and reactant $\sigma_P^{\uparrow} l/\omega\rho_0 = \sigma_R^{\uparrow} l/\omega\rho_0 = 0.1, 1, 10$ and strength of surface tension effects of reactant and product $\Gamma_P\rho_{0,P}/\Gamma_R\rho_{0,R} = 1/2, 1, 2$. The color scheme of the background indicates the fastest growing mode wavenumber q_{max} obtained from linear stability analysis divided by the passive case fastest growing wavenumber $q_{max,p}$ ranging from stable films $q_{max} = 0$ in brown to the most excited states in dark blue. The symbols in the foreground correspond to simulations started from the initial condition $h = h_0 + \mathcal{N}$, $\rho = \rho_0$, $\rho_P = \rho_{0,P}$, $\rho_R = \rho_{0,R}$ and all relevant parameters but the sorption rates are chosen as reported in the Experimental Section. Red and magenta symbols indicate film rupture, while orange and pink symbols indicate excitement of certain wavelengths but no film rupture. In green simulations confirming a stable homogeneous state are reported. The marker shapes correspond to different observed steady state behavior, exemplary shown by simulation snapshots at the top. The diagram highlighted in dark green corresponds to that reported in Figure 2. The left *y*-axis of the diagrams is $\tilde{\Gamma}_P$, the right *y*-axis is $\tilde{\Gamma}_R$ and scales as $\Gamma_P\rho_{0,P}/\Gamma_R\rho_{0,R}$ times the left *y*-axis. The *x*-axis of the diagrams is αh_0. The black lines identify the boundary between oscillations (above) and steady state (below) according to LSA.

by the evaporation term of the evolution equation of ρ_P Equation (4) $\sigma_P^{\uparrow}\rho_P l/h$. The measured values are reported in **Figure 8**.

As a general trend, we observe that for lower evaporation rates of the reactant, and thus, at higher concentrations of reactant inside the liquid film, the catalytic yield is higher. Therefore, for the diagrams reported on the left of Figure 8, the catalytic yield is higher than on the right. Further, we observe that for parameters for which the liquid film stays closed, there is a higher yield than for parameters with the same sorption for which the film breaks. Most interestingly, for $\sigma_P^{\uparrow} l/\omega\rho_0 \ll 1$ (left row), a vertically homogeneously distributed catalyst ($\alpha = 0$) produces a higher catalytic yield than the catalyst that is attracted to the liquid-gas interface. This is due to the fact that, in this regime, when the catalysts accumulate at the fluid interface, $\alpha h_0 < 0$, they also form clusters due to the Marangoni flows (see the peaks in Figure 7a). This additional aggregation along the interface generates a depletion of reactants and hence a reduction of the overall yield. Similar dynamics also happen for $\alpha h_0 > 0$; see, for example, the depletion of reactants in Figure 6c.

3. Discussion

3.1. Significance and Implications

Our theoretical analysis pinpoints the transverse distribution of catalysts (captured by α) and the net effect of the chemicals on the surface tension ($\Gamma_{R,P}\rho_{R,P}$) as the key parameters. Therefore, to derive conclusions that are relevant for real systems, it is crucial

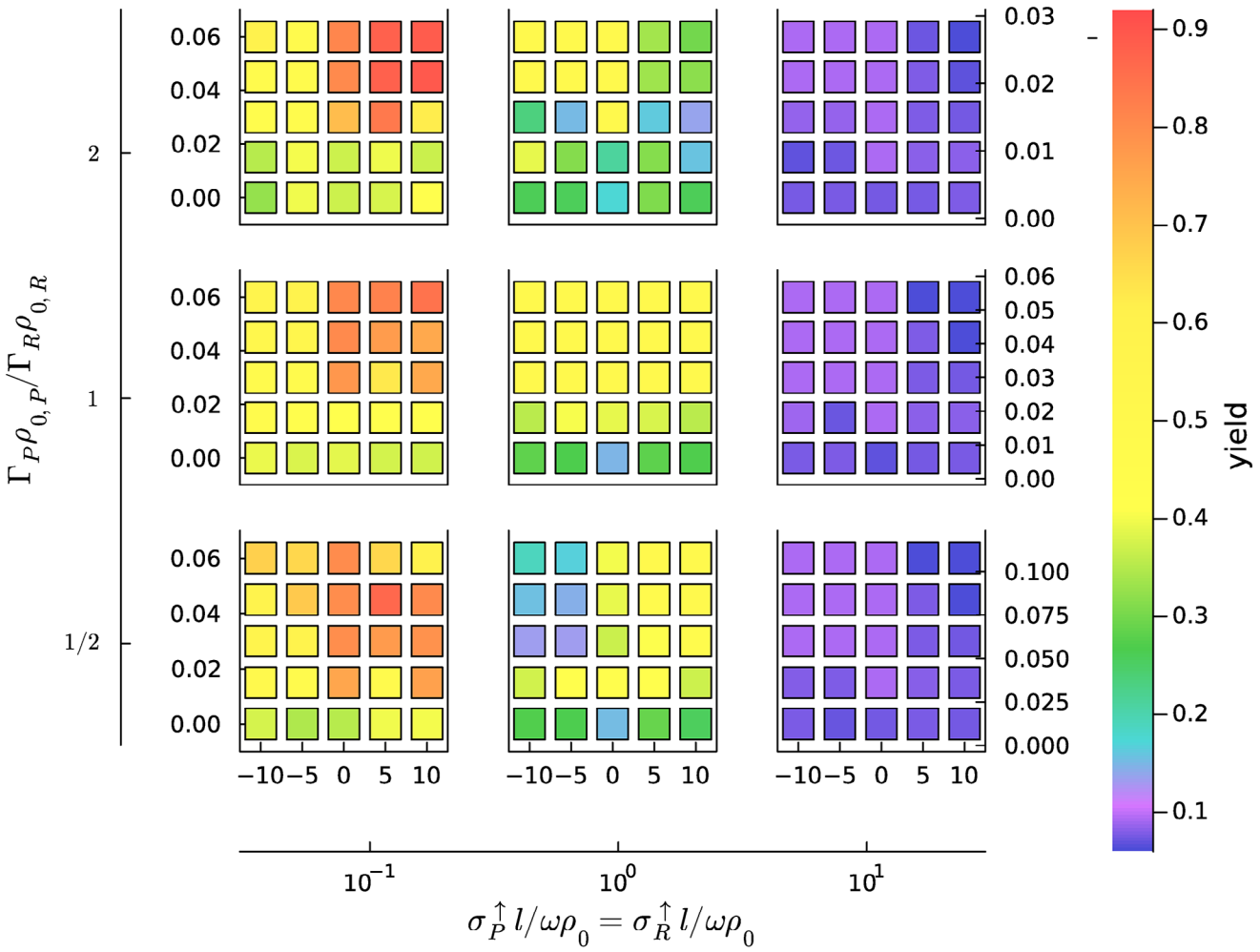

Figure 8. Catalytic yield depending on sorption and strength of surface tension effects, reported as $\int \sigma_P^{\uparrow}\rho_P l/hdx/(\sigma_R^{\downarrow}\rho_{BRes}L)$. The nine plots show the catalytic for different ratios of the surface tension effects of reactant and product $\Gamma_P\rho_{0,P}/\Gamma_R\rho_{0,R} = 1/2,\ 1,\ 2$ and sorption rates of product and reactant $\sigma_P^{\uparrow} l/\omega\rho_0 = \sigma_R^{\uparrow} l/\omega\rho_0 = 0.1,\ 1,\ 10$. The color of the markers reports the measured catalytic yield in simulation units. The left *y*-axis of the diagrams is $\tilde{\Gamma}_P$, the right *y*-axis is $\tilde{\Gamma}_R$ and scales as $\Gamma_P\rho_{0,P}/\Gamma_R\rho_{0,R}$ times the left *y*-axis. The *x*-axis of the diagrams is αh_0. The parameters of the simulations presented in this figure correspond to the simulation parameters used in Figure 7.

to bind the range of these parameters via available experimental values.

For what concerns the tunability of the transverse distribution of catalysts, encoded by α, experimental measurements have reported accumulation of catalysts at both liquid–gas[45,59,60] ($\alpha < 0$) and solid–liquid[29,45] ($\alpha > 0$) interfaces. On top of this, electric fields can be used to tune both the distribution of particles in a thin film as well as the range within which the disjoining pressure is operational[61] (Ref. [61] shows that applying a voltage of up to $60V$ disjoining pressure becomes relevant for a film of thickness as large as $10\mu m$. In such a scenario with a micrometer-thick film being prone to spinodal rupture it is possible to have catalytic particles that can be easily tracked by optical methods making it possible to observe the dynamics of the catalyst distribution experimentally while having a relevant effect from the disjoining pressure augmented by the electrical potential. In Ref. [62] the authors show how to include such effects into the lubrication-approximation approach).

For what concerns the magnitude of $\Gamma_{R,P}\rho_{R,P}l/h_0$ as compared to the bare value γ_0, recent measurements[33] show that the surface tension of two selected ILs is significantly affected by the applied gas pressure and thus by the concentration of the dissolved gas in the liquid phase (also reported in Figure S7, Supporting Information). In particular, in the case of carbon dioxide (CO_2) as an example of reactant gas, a gas pressure of 1MPa, for example, reduces the vapor-liquid surface tension of the ILs [OMIM][PF_6] or [m(PEG_2)$_2$IM]I by about 10% for a temperature of 303.15K. This relative change is smaller in the case of argon (Ar) gas, where a decrease in the surface tension of about 2.5% relative to the values for the pure ILs could be determined experimentally. These values are compatible with those used to derive Figure 2 which shows that indeed even a few percent variation in the local surface tension is sufficient to observe the novel regimes predicted by our model.

The experimental data that we have commented on supports that, upon varying the concentration of the suspended

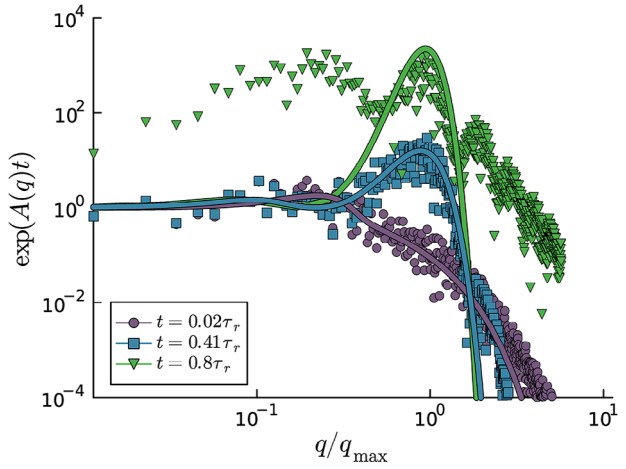

Figure 9. Comparison between the spectrum of the profile of a thin liquid film containing catalyst, reactant, and product species obtained from a simulation (points) with the linear solution (16) (lines) shows good agreement at various times. Different times are depicted by varying color and given in fractions of the rupture time τ_r defined in (12). L is the simulation box size.

chemicals, surface tension is influenced by magnitudes as large as the magnitudes studied above. However, they do not show that such changes in densities (and hence in surface tension) can be attained utilizing chemical reactions which is indeed crucial in our model. On top of this, our predictions pinpoint the relevance of concentrations of chemicals. To estimate the magnitude of the local variations in chemical densities we recall that the mean concentration of product in the film is given by $\rho_{0,P} = \frac{\omega\rho_0}{\sigma_P^{\uparrow} l} \frac{\rho_{R,Res}\sigma_R^{\downarrow} h_0}{\omega\rho_0 + \sigma_R^{\uparrow} l}$. Thus the amount of dissolved product in the liquid is proportional to the concentration of reactants in the atmosphere $\rho_{R,\,Res}$ which itself is proportional to the gas pressure of reactant. We calculate the mean concentration of reactant inside the film to be $\rho_{0,R} = \frac{\rho_{R,Res}\sigma_R^{\downarrow} h_0}{\sigma_R^{\uparrow} l + \omega\rho_0}$. There are two regimes of interest here: First, if $\omega\rho_0 \gg \sigma_R^{\uparrow} l$ then $\rho_{0,P} \approx \rho_{R,Res} \frac{\sigma_R^{\downarrow} h_0}{\sigma_P^{\uparrow} l}$ and thus $\rho_{0,\,P}$ can be controlled by either increasing the gas pressure of reactant R or by the ratio of the rates $\frac{\sigma_R^{\downarrow}}{\sigma_P^{\uparrow}}$. It is reasonable to assume that the sorption of reactant and product are comparable, and thus, the concentrations of reactant and product are alike. Second, if $\omega\rho_0 \ll \sigma_R^{\uparrow} l$ we obtain $\rho_{0,P} \approx \frac{\omega\rho_0}{\sigma_P^{\uparrow} l} \rho_{R,Res} \frac{\sigma_R^{\downarrow} h_0}{\sigma_P^{\uparrow} l}$ resulting in an amplification factor $\frac{\omega\rho_0}{\sigma_P^{\uparrow} l}$. In fact, if $\sigma_P^{\uparrow} l \ll \omega\rho_0 \ll \sigma_R^{\uparrow} l$ we have that $\frac{\omega\rho_0}{\sigma_P^{\uparrow} l} \gg 1$ and thus $\rho_{0,\,P} \gg \rho_{0,\,R}$. Accordingly, if the product is much less volatile than the reactant, significant changes in the vapor-liquid surface tension relative to that of the pure IL can also be achieved for lower gas pressures of the reactant.

3.2. Conclusion

We have developed a continuum model to describe the dynamics of a chemically reactive thin liquid films within which the chemical reactions are triggered by catalysts. In particular, we have characterized the stability of the film upon changing the distribution of catalyst across the film.

We analyzed the model in terms of its linear stability and obtained predictions on the persistence of ultra-thin liquid layers as well as the time scales of the evolution of such films. That revealed a surprisingly rich phenomenology, reaching from the stabilization of an otherwise unstable film, due to the overall reduction of the vapor-liquid surface tension and Marangoni flows, over the tuning of its dominant wavelength to the accumulation of catalytic particles which is in qualitative agreement with experimental observations.[10] Not only the stability, but also the time scale needed to attain the steady state are strongly affected by the chemical reactions and, as shown in Figure 5, the rupture time can be orders of magnitude larger as compared to the passive case. This is crucial for the design of measurement techniques studying film dynamics as well as for the design and optimization of catalytic materials.

The predictions of the LSA have been confirmed by numerical simulations with a LBM scheme. In particular, the numerical data shed further light on the evolution of our model system. In fact, by numerical inspection, we found that in addition to stable films with homogeneous height, and spherical-cap droplets, other eventual regimes can be attained, such as films with inhomogeneous heights, non-spherical droplets (see Figure 6) as well as unsteady states such as traveling and stationary waves (see Figure 7). Since thin liquid films ae xploited in the case of SLP SILP reactors, we have characterized the catalytic yield in the different scenarios that we have identified. Surprisingly, our model predicts that, due to the onset of Marangoni flows, accumulation of catalysts at the fluid interface may hinder the yield as compared to the case of catalysts homogeneously distributed in the film. Remarkably, such a prediction is in line with our experimental measurements.

All these numerical data have been obtained in the range of parameters that are compatible with current experimental measurements of both the transverse distribution of catalysts as well as the sensitivity of surface tension to added reactant chemicals such as dissolved gases. Hence we expect our prediction to be relevant in the design of novel catalysis concepts such as SLP and SILP technologies.

4. Experimental Section

Linear Stability Analysis (LSA): In order to study the system, (1), (7), (4) and (3) are linearized by expanding them around the homogeneous state $h = h_0 + \delta h$, $\rho = \rho_0 + \delta\rho$, $\rho_P = \rho_{0,\,P} + \delta\rho_P$, $\rho_R 0\rho_{0,\,R} + \delta\rho_R$ and retaining only linear terms in the perturbations. By performing Fourier transformations according to $\widehat{\delta\rho} = \hat{\rho}, \widehat{\delta h} = \hat{h}, \widehat{\rho_P} = \widehat{\delta\rho_P}, \widehat{\rho_R} = \widehat{\delta\rho_R}$ the resulting expression is

$$\partial_t \begin{pmatrix} \hat{h} \\ \hat{\rho} \\ \widehat{\rho_P} \\ \widehat{\rho_R} \end{pmatrix} = A(q) \cdot \begin{pmatrix} \hat{h} \\ \hat{\rho} \\ \widehat{\rho_P} \\ \widehat{\rho_R} \end{pmatrix} \tag{15}$$

The matrix $A(q)$ and the details of this computation can be found in the Supporting Information. This system was solved to obtain the linear solution

$$\begin{pmatrix} \hat{h} \\ \hat{\rho} \\ \widehat{\rho_P} \\ \widehat{\rho_R} \end{pmatrix} (q,t) = \begin{pmatrix} \hat{h} \\ \hat{\rho} \\ \widehat{\rho_P} \\ \widehat{\rho_R} \end{pmatrix} (q,0) e^{A(q)t} \tag{16}$$

In **Figure 9**, the linear solution was validated according to (16) against the spectrum of a numerical solution of the full model Equations (1–4) and (7). This solution was obtained by a lattice Boltzmann method for the TFE developed by Refs. [53, 63, 64] and is explained in detail in the Supporting Information. The initial condition chosen in the simulation are homogeneous fields with a small perturbation $h(\mathbf{x}) = h_0 + \epsilon\mathcal{N}$, $\rho(\mathbf{x}) = \rho_0$, $\rho_R = \rho_{0,R} := \rho_{R,Res}\sigma_R^{\downarrow}h_0/(\omega\rho_0 + \sigma_R^{\uparrow}l)$, $\rho_P = \rho_{0,P} := \omega\rho_{0,R}\rho_0/(\sigma_P^{\uparrow}l)$. Here ϵ is a number such that $\epsilon \ll h_0$ and $\mathcal{N}$ is a normal distributed random variable. The linear solution performs well for short time scales, deteriorating as approach film rupture. However, it still accurately captures the maxima of the film height spectrum, as shown in Figure 9. Equation (16) was utilized to predict types of behaviors of the system and compare them against the numerical solution of the full model. Specifically, we focus on the eigenvalues $\eta_m(q)$ and $\eta_{2,3,4}$ of the matrix $A(q)$, where the indices were chosen such that $\eta_m > \eta_{2,3,4}$. The wavenumber q is defined at which η_m achieves its maximum positive value as the fastest growing mode, denoted as $q_{\max}$:

$$q_{\max} := \operatorname{argmax}(\eta_m) \tag{17}$$

As demonstrated, $q_{\max}$ and max (η_m) effectively capture the system's stability and rupture time.

Simulation Parameters: Parameters are chosen if not stated differently $R_c = 1\text{nm}$, $R_P = 0.5\text{Å}$, $h_0 = 10\text{nm}$, $\nu = 8.9 \cdot 10^{-6}\text{m}^2/\text{s}$, $\rho_l = 10^3\text{kg/m}^3$, $\gamma_0 = 0.073\text{N/m}$, $\theta_0 = \pi/9$, $\omega\rho_0/h_0 = 1.6 \cdot 10^6 s^{-1}$, $\sigma_P l/h_0^{\uparrow} = \sigma_R^{\uparrow}l/h_0 = 1.6 \cdot 10^6 1/\text{s}$, $\sigma_R^{\downarrow} = 1.6 \cdot 10^7 1/\text{s}$, $h^* = 0.1h_0$, $h_0\alpha = 5$, $\tilde{\Gamma}_P = 2\tilde{\Gamma}_R = 0.03$. Surface tension,[65] density,[66] and viscosity[67] were chosen to match the values of water at $T = 303\text{K}$. The reaction rate ω was derived from Ref. [68], where spherical catalyst particles coated with platinum suspended in a 10% aqueous H_2O_2 solution consume $0.0212\text{mol}/(\text{sm}^2)$ H_2O_2 molecules on their active sites. Here, these values were used and it was assumed that catalyst particles were 1nm in radius and suspended at a 4% volume fraction. To reduce the number of free parameters, the transfer rates were set $\sigma_P^{\uparrow}l/h_0 = \sigma_R^{\uparrow}l/h_0 = \omega\rho_0/h_0 = 1.6 \cdot 10^6 s^{-1}$, and $\sigma_R^{\downarrow} = 10\omega\rho_0 = 1.6 \cdot 10^7 s^{-1}$ for most parts if not stated otherwise.

Supporting Information

Supporting Information is available from the Wiley Online Library or from the author.

Acknowledgements

The authors acknowledge funding by the Deutsche Forschungsgemeinschaft (DFG, German Research Foundation) Project-ID 431791331–SFB 1452, the Helmholtz Association of German Research Centers (HGF) and the Federal Ministry of Education and Research (BMBF), Germany for supporting the Innovation Pool project "Solar H2: Highly Pure and Compressed," and Stefan Zitz for fruitful discussions.

Conflict of Interest

The authors declare no conflict of interest.

Data Availability Statement

The data that support the findings of this study are openly available in Chemically reactive thin films: dynamics and stability – Data at https://doi.org/10.5281/zenodo.10691669, reference number 10691669.

Keywords

non-equilibrium dynamics, supported liquid phase catalysis, thin film equation, wetting

Received: October 22, 2024
Revised: January 10, 2025
Published online: March 17, 2025

[1] Z. Wei, Y. Li, R. G. Cooks, X. Yan, *Annu. Rev. Phys. Chem.* **2020**, *71*, 31.
[2] A. Fallah-Araghi, K. Meguellati, J.-C. Baret, A. E. Harrak, T. Mangeat, M. Karplus, S. Ladame, C. M. Marques, A. D. Griffiths, *Phys. Rev. Lett.* **2014**, *112*, 028301.
[3] R. M. Bain, C. J. Pulliam, F. Thery, R. G. Cooks, *Angew. Chem. Int. Ed.* **2016**, *55*, 10478.
[4] Y. Li, Y. Liu, H. Gao, R. Helmy, W. P. Wuelfing, C. J. Welch, R. G. Cooks, *Chem. - Eur. J.* **2018**, *24*, 7349.
[5] R. Shi, L. Shang, C. Zhou, Y. Zhao, T. Zhang, *Exploration* **2022**, *2*, 20210046.
[6] V. Buch, A. Milet, R. Vácha, P. Jungwirth, J. P. Devlin, *Proc. Natl. Acad. Sci.* **2007**, *104*, 7342.
[7] P. B. Petersen, R. J. Saykally, *Chem. Phys. Lett.* **2008**, *458*, 255.
[8] M. F. Ruiz-Lopez, J. S. Francisco, M. T. C. Martins-Costa, J. M. Anglada, *Nat. Rev. Chem.* **2020**, *4*, 459.
[9] S. Mondal, S. Acharya, R. Biswas, B. Bagchi, R. N. Zare, *J. Chem. Phys.* **2018**, *148*, 244704.
[10] D. P. Singh, A. Domínguez, U. Choudhury, S. N. Kottapalli, M. N. Popescu, S. Dietrich, P. Fischer, *Nat. Commun.* **2020**, *11*, 2210.
[11] Z. Wei, X. Zhang, J. Wang, S. Zhang, X. Zhang, R. G. Cooks, *Chem. Sci.* **2018**, *9*, 7779.
[12] F. Zhao, S.-i. Fujita, M. Arai, *Curr. Org. Chem.* **2006**, *10*, 1681.
[13] K. Zeng, Z. Huang, J. Yang, Y. Gu, *Chin. J. Catal.* **2015**, *36*, 1606.
[14] W. Alsalahi, A. Trzeciak, *Coord. Chem. Rev.* **2021**, *430*, 213732.
[15] M. Schörner, P. Rothgießer, K. Mitländer, D. Wisser, M. Thommes, M. Haumann, *ChemCatChem* **2021**, *13*, 4192.
[16] J. D. Scholten, B. C. Leal, J. Dupont, *ACS Catal.* **2012**, *2*, 184.
[17] H. Masoud, H. A. Stone, *J. Fluid Mech.* **2014**, *741*, R4.
[18] A. Domínguez, P. Malgaretti, M. Popescu, S. Dietrich, *Phys. Rev. Lett.* **2016**, *116*, 078301.
[19] S. Jafari Kang, S. Sur, J. P. Rothstein, H. Masoud, *Phys. Rev. Fluids* **2020**, *5*, 084004.
[20] A. Squarcini, P. Malgaretti, *J. Chem. Phys.* **2020**, *153*, 234903.
[21] S. Imamura, T. Kawakatsu, *Eur. Phys. J. E* **2021**, *44*, 127.
[22] H.-P. Steinrück, P. Wasserscheid, *Catal. Lett.* **2015**, *145*, 380.
[23] M. H. Rasmus Fehrmann, A. Riisager, *Supported Ionic Liquids*, Wiley, New York **2014**.
[24] M. Hatanaka, T. Yasuda, E. Uchiage, M. Nishida, K.-i. Tominaga, *ACS Sustainable Chem. Eng.* **2021**, *9*, 11674.
[25] J. M. Marinkovic, A. Riisager, R. Franke, P. Wasserscheid, M. Haumann, *Ind. Eng. Chem. Res.* **2019**, *58*, 2409.
[26] Y. Gu, G. Li, *Adv. Synth. Catal.* **2009**, *351*, 817.
[27] A. Riisager, R. Fehrmann, S. Flicker, R. Van Hal, M. Haumann, P. Wasserscheid, *Angew. Chem. Int. Ed.* **2005**, *44*, 815.
[28] R. Knapp, A. Jentys, J. A. Lercher, *Green Chem.* **2009**, *11*, 656.
[29] M. Frosch, C. L. Tavera Mendez, A. B. Koch, M. Schörner, M. Haumann, M. Hartmann, D. Wisser, *J. Phys. Chem. C* **2023**, *127*, 9196.
[30] A. Pereira, P. M. J. Trevelyan, U. Thiele, S. Kalliadasis, *J. Eng. Math.* **2007**, *59*, 207.
[31] A. Pereira, P. M. J. Trevelyan, U. Thiele, S. Kalliadasis, *Phys. Fluids* **2007**, *19*, 112102.
[32] A. Bender, P. Stephan, T. Gambaryan-Roisman, *Phys. Rev. Fluids* **2017**, *2*, 084002.
[33] Z. Zhai, T. M. Koller, *J. Mol. Liq.* **2023**, *377*, 121491.
[34] A. Oron, S. H. Davis, S. G. Bankoff, *Rev. Mod. Phys.* **1997**, *69*, 931.
[35] R. V. Craster, O. K. Matar, *Rev. Mod. Phys.* **2009**, *81*, 1131.
[36] R. Zwanzig, *J. Phys. Chem.* **1992**, *96*, 3926.
[37] D. Reguera, J. M. Rubi, *Phys. Rev. E* **2001**, *64*, 061106.

[38] P. Malgaretti, I. Pagonabarraga, J. Rubi, *Front. Phys.* **2013**, *1*, 21.
[39] P. Malgaretti, J. Harting, *Entropy* **2023**, *25*, 470.
[40] U. Thiele, *Eur. Phys. J. Spec. Top.* **2011**, *197*, 213.
[41] U. Thiele, D. V. Todorova, H. Lopez, *Phys. Rev. Lett.* **2013**, *111*, 117801.
[42] X. Xu, U. Thiele, T. Qian, *J. Phys.: Condens. Matter* **2015**, *27*, 085005.
[43] P. Malgaretti, M. Janssen, I. Pagonabarraga, J. M. Rubi, *J. Chem. Phys.* **2019**, *151*, 084902.
[44] Additional electrostatic interactions between with the solid surface can be accounted for by changing the term $\mathcal{F}_0$ accordingly.[43]
[45] H.-P. Steinrück, J. Libuda, P. Wasserscheid, T. Cremer, C. Kolbeck, M. Laurin, F. Maier, M. Sobota, P. S. Schulz, M. Stark, *Adv. Mater.* **2011**, *23*, 2571.
[46] S. K. Antara, D. Hemmeter, Z. Zhai, D. Kremitzl, F. Maier, T. M. Koller, H.-P. Steinrück, M. Haumann, *ChemCatChem* **2024**, 202400574.
[47] S. Shylesh, D. Hanna, A. Mlinar, X.-Q. Kong, J. A. Reimer, A. T. Bell, *ACS Catal.* **2013**, *3*, 348.
[48] In the case of charged surfaces and charged catalysts, $\beta\xi$ is related to the electrostatic potential.
[49] A. Vrij, *Discuss. Faraday Soc.* **1966**, *42*, 23.
[50] M. Doi, *Soft Matter Physics*, Oxford University Press, USA **2013**.
[51] M. Rauscher, R. Blossey, A. Münch, B. Wagner, *Langmuir* **2008**, *24*, 12290.
[52] R. Fetzer, M. Rauscher, R. Seemann, K. Jacobs, K. Mecke, *Phys. Rev. Lett.* **2007**, *99*, 114503.
[53] S. Zitz, A. Scagliarini, J. Harting, *Phys. Rev. E* **2021**, *104*, 034801.
[54] F. Pelusi, M. Sega, J. Harting, *Phys. Fluids* **2022**, *34*, 062109.
[55] A. Riisager, R. Fehrmann, M. Haumann, P. Wasserscheid, *Top. Catal.* **2006**, *40*, 91.
[56] P.-G. De Gennes, F. Brochard-Wyart, D. Quéré, *Capillarity and Wetting Phenomena*, Springer New York, New York, NY **2004**.
[57] M. A. Herrero, J. J. Velázquez, *JOMB* **1996**, *35*, 177.
[58] A. Winter, Y. Liu, A. Ziepke, G. Dadunashvili, E. Frey, *arXiv preprint arXiv:2409.16049* **2024**.
[59] D. Hemmeter, D. Kremitzl, P. S. Schulz, P. Wasserscheid, F. Maier, H. Steinrück, *Chem. - Eur. J.* **2023**, *29*, 202203325.
[60] D. Hemmeter, U. Paap, F. Maier, H.-P. Steinrück, *Catalysts* **2023**, *13*, 871.
[61] B. Bhatt, S. Gupta, V. Sumathi, S. Chandran, K. Khare, *Adv. Mater. Interfaces* **2023**, *10*, 2202063.
[62] K. John, P. Hänggi, U. Thiele, *Soft Matter* **2008**, *4*, 1183.
[63] S. Zitz, A. Scagliarini, S. Maddu, A. A. Darhuber, J. Harting, *Phys. Rev. E* **2019**, *100*, 033313.
[64] S. Zitz, A. Scagliarini, J. Harting, *Phys. Rev. Fluids* **2023**, *8*, L122001.
[65] P. T., *The International Association for the Properties of Water and Steam* **2014**.
[66] W. Wagner, A. Pruß, *J. Phys. Chem. Ref. Data* **2002**, *31*, 387.
[67] M. L. Huber, R. A. Perkins, A. Laesecke, D. G. Friend, J. V. Sengers, M. J. Assael, I. N. Metaxa, E. Vogel, R. Mareš, K. Miyagawa, *J. Phys. Chem. Ref. Data* **2009**, *38*, 101.
[68] A. Brown, W. Poon, *Soft Matter* **2014**, *10*, 4016.